Arc expansion in xenon flashlamps

M. J. Kushner

Spectra Technology, Inc.[a], 2755 Northup Way, Bellevue, Washington 98004

Plasma arcs in large diameter ($d > 1$ cm) xenon flashlamps often do not completely fill the bore of the discharge tube. The arc is usually initiated on one side of the discharge tube, adjacent to the ground plane, and the fraction of the discharge tube filled with plasma varies as a function of axial location. A model is presented that describes, from first principles, arc expansion in xenon flashlamps. The model simultaneously solves a coupled set of one-dimensional transport equations in different regions of the discharge tube to simulate two-dimensional effects in hydrodynamics, electron kinetics, and radiation transport. Using this method, expansion of arcs initiated at arbitrary locations within the discharge tube can be studied. Arc filling fractions are found to decrease with increasing filling pressure of xenon, increasing diameter of the discharge tube, and decreasing stored energy in the discharge circuit. The arc filling fraction also decreases as the breakdown filament moves away from the axis of the discharge tube and towards the wall. Arc expansion is slowed and ultimately halted by a lowered E/N (electric field/gas density) in the gas exterior to the arc, rapid conversion of atomic ions to molecular ions and their subsequent recombination, and by the efficient manner in which radiation dissipates energy which might otherwise be available for thermodynamic expansion of the arc. The asymmetric expansion of the plasma arc results in asymmetric heating of the inside wall of the discharge tube, also calculated in the model. The growth of the plasma arc is also found to be in part responsible for changes in the spectrum of radiation emitted from the arc for various angles of observation. This effect results from wavelength-dependent absorption coefficients in the plasma.

I. INTRODUCTION

The operating characteristics of xenon flashlamps (e.g., current, voltage, emission spectrum) have been successively described by empirical and semiempirical relationships and models.[1–14] The basis of some of these models is that the plasma arc of the flashlamp is in local thermodynamic equilibrium (LTE). This approximation is quite good for fully or nearly fully developed arcs in which the plasma conditions have reached a quasi-steady state. These models, though, are incapable of describing from first principles the transient arc formation state of the discharge, or any position dependent phenomenon.

The fact that arcs in xenon flashlamps do not completely fill the flashlamp bore has been reported by many investigators.[15–19] Specifically, the arc is usually initiated on one side of the flashlamp and expands in a nonradially symmetric fashion.[16–19] After the arc has expanded to its maximum extent, the fraction of the cross-sectional area of the bore that is filled by plasma is not uniform along the axis. This fraction, defined as the bore filling fraction, has a sinusoidal-like modulation as a function of axial position. The modulation has a period of about a half to a few centimeters. The origin of the axial modulation of the bore filling fraction can be found in the method of initiation of the arc.

The self-sustaining voltage of a xenon flashlamp having a current density of 2500 A/cm^2 and having a diameter of 1.5 cm is about 60 V/(cm atm).[16] In the absence of a dc keep-alive or simmer current, this voltage is insufficient to break down the initially neutral gas. To initiate breakdown of the flashlamp plasma, a peaking capacitor is usually incorporated into the circuit. The purpose of this capacitor is to ring the applied voltage to a value sufficiently high to break down the gas. Since the purpose of using a flashlamp would be defeated by enclosing the discharge tube within a coaxial current return, the ground plane is not symmetric with respect to the axis of the discharge tube. The ground plane is usually the relatively flat reflecting surface placed close to one side of the lamp or a trigger wire attached to one side of the tube.

When a high potential is initially applied to one of the electrodes and there is no plasma, the electric field lines are directed from the electrode to the ground plane. The initial breakdown filament that develops tends to align itself along these field lines and therefore propagates towards the side of the discharge tube closest to the ground plane. (See Fig. 1.) As a high plasma density forms near the wall, a sheath develops at the boundary.[19] The field lines are bent around the non-neutral sheath and aligned more or less parallel to the discharge tube wall and collinear with the axis of the tube, thereby also directing the filament down the tube. When the breakdown filament propagates beyond the sheath region, it is again directed by the electric field towards the wall. This process repeats as the breakdown filament "skips" down the side of the discharge tube in an oscillatory fashion until the opposite electrode is reached. At this point a sheath shields
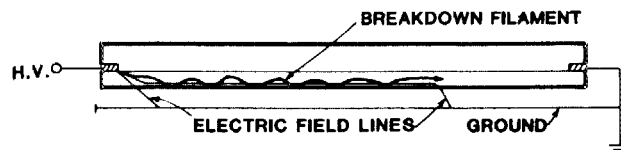

FIG. 1. Schematic representation of propagation of the initial breakdown filament. In the absence of a plasma, the electric field lines direct the breakdown filament towards the ground plane located on one side of the discharge tube. As a sheath begins to form at the wall, the electric field lines are bent parallel to the wall directing the breakdown filament in that direction along the axis of the discharge tube.

---

[a] Formerly Mathematical Sciences Northwest, Inc.

the interior of the discharge tube from the ground plane, therefore bending the electric field lines in such a manner that the maximum electric field is aligned along the axis of the discharge tube for the entire length of the plasma. The imprint of the oscillatory motion of the breakdown filament is preserved in the shape of the fully expanded plasma, the manifestation of which is the sinusoidally modulated bore filling fraction. We will see that the arc filling fraction at a particular axial location is characterized by the radial coordinate of the breakdown filament at the axial point. In general, the bore filling fraction decreases as the location of the breakdown filament moves away from the axis of the discharge tube.

Clearly, a complete description of the process by which a narrow breakdown filament expands to form an arc and fill the discharge tube requires a fully three-dimensional, time-dependent hydrodynamic and plasma kinetics model. The interior of the arc may be well described by assuming local thermodynamic equilibrium while the edge of the expanding arc channel is definitely not in equilibrium. The model must therefore be capable of describing the transition of the state of the gas from initially cold conditions, through an electron kinetics dominated phase, and ultimately into a LTE phase. All of these conditions may exist at different locations in the flashlamp tube at the same instant in time.

In this paper, a model will be described which is an attempt at a first principles description of the arc formation phase of a xenon flashlamp, from initial breakdown filament to fully developed arc. No assumptions are made concerning LTE conditions. The model is time and spatially dependent, and includes heavy particle hydrodynamics, electron collision kinetics, radiation transport, and an external electrical circuit. A full three-dimensional theoretical formulation of the problem was beyond the scope of this study. The pertinent physics, though, can be studied by a treatment we have chosen to call "sector space." With this method, the computation time increases only linearly with the inverse of the mesh spacing as opposed to the inverse of the square of the mesh spacing.

In Sec. II of this paper, the sector space method is described, and the details of the kinetics, electrical and radiation transport portions of the model are described. In Sec. III, the model is applied to calculate arc formation rates and other properties for large bore, subatmospheric pressure lamps. The flashlamps of interest for the model are of the type used in large, fusion class Nd-glass laser amplifiers.[16] The typical dimensions are 2-cm-i.d., 50-cm arc length, and xenon fill pressure of 300 Torr. Concluding remarks are contained in Sec. IV.

II. DESCRIPTION OF THE PLASMA BORE FILLING MODEL

A. Sector space formulation

For arcs whose breakdown filaments are aligned along the axis of the discharge tube, a radially symmetric calculation is sufficient. For arcs initiated off-axis a more detailed computational method is required. The method used in this model is called sector space. In the sector space formulation, a point within the discharge tube is specified as the location

at which the breakdown filament passes through the radial-azimuthal plane for a given axial point. (See Fig. 2.) This location defines the local point of symmetry for that axial coordinate. Emanating from the center of symmetry are radial spokes of different lengths which terminate at the discharge tube wall and define the center of a sector. The azimuthal extent, measured from center of symmetry, of each sector is the same. A separate set of one-dimensional, time-dependent partial differential equations describing the pertinent hydrodynamics and plasma kinetics are simultaneously integrated along each of the sectors' radial spokes. If not for the coupling of each sector through the boundary conditions, discussed below, each of these sectors would appear to be plasmas expanding in discharge tubes of different radii. The weaknesses of this formulation are that the center of symmetry may migrate during the arc expansion process and that the direct exchange of mass between adjacent sectors resulting from azimuthal convection (as referenced to the nonaxial center of symmetry) can only be approximated.

The sectors are coupled through the boundary conditions, through radiation transport, and indirectly through the response of the discharge circuit. The most stringent boundary conditions are that the hydrodynamic and kinetic variables for all sectors must be equal at the center of symmetry and that the volume (sector) averaged mass density must be identical to the initial conditions (conservation of mass). The latter condition is manifested through our approximate treatment of azimuthal convection. Azimuthal convection is approximated by allowing the thermodynamic pressures of adjacent sectors to equilibrate on a timescale commensurate with the local sound speed. For example if one of two isolated sectors is independently heated, its density is reduced and its partner's density increased in such a manner to equilibrate pressures. Azimuthal convection is approximated on only a sector-to-sector basis. That is, mass is exchanged between sectors as a whole, as opposed to exchanging mass between mesh points at the same radius in neighboring sectors.

The different sectors also communicate through the discharge circuitry. For the purpose of calculating the impedance of the flashlamp, each sector can be viewed as being
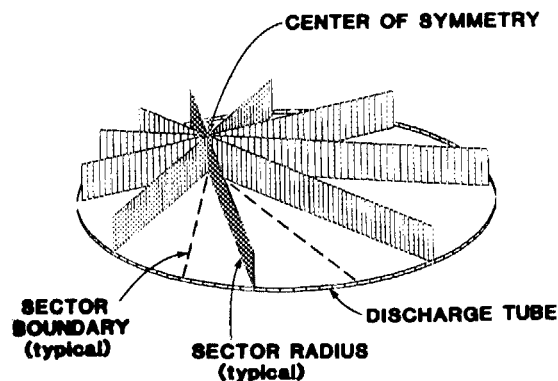

FIG. 2. Schematic diagram of the "sector space" formulation. The center of symmetry is the point in the radial-azimuthal plane through which the breakdown filament passes. Spokes of different lengths emanating from the center of symmetry define the center of their respective sectors. Each sector has the same azimuthal extent as measured from the center of symmetry.

one of a set of parallel resistors. The resistance of the ith sector is given by

$$R_i = \frac{lm}{\int_{A_i} \frac{ne^2}{\nu_c} dA},$$ (1)

where n is the electron density, m is the electron mass, ν_c is the electron collision frequency, l is the arc length, and the integral is performed over the area of the arc associated with the ith sector. In practice, this integral is replaced by a summation over mesh points within that sector. If during the development of the arc one sector happens to become more conductive than the others, the impedance of the arc decreases proportionally. This in turn decreases the axial voltage drop across the arc and therefore the local electric field for all the sectors. Since the force function for expansion of the plasma in each sector is gas heating, which is ultimately driven by the applied electric field, rapid arc expansion in one sector, and subsequent impedance collapse of the discharge, inhibits the rate of arc expansion in the other sectors.

The various sectors are also coupled through radiation transport, which is explicitly included in the model (and described in detail below). For times later than about 100 μs after breakdown, the radiation is mostly continuum. The dominant source of continuum radiation can be shown to result from free-bound radiative recombination. Similarly, the dominant absorption mechanism is bound-free photoionization. Radiation emitted in one sector can be absorbed in a different sector, thereby changing the local rate of ionization and influencing the absorbing sector's rate of arc expansion.

B. Electron kinetics and heavy particle hydrodynamics

Along each sector, and at each mesh point of each sector, the following species were included in the model: electron temperature (T_e), heavy particle temperature (T_g), charged particle density (n), heavy particle density (N), xenon excited states and molecular densities (see below), and heavy particle momentum (ρu). The voltages and currents associated with the external circuit elements are global variables (see below).

The electron distribution function was assumed to be a Maxwellian and electron transport was verified to be accurately described by the ambipolar approximation.[20] In ambipolar diffusion, the radial electric field is solved for by specifying that the radial flux of electrons must equal that of ions. This approximation is valid for charged particle densities in excess of about 10^9 cm^{-3}.[21] The charged particle density is in excess of 10^{16} cm^{-3} at all points in the arc except in the transition region between the arc and the cold neutral gas exterior to the arc. In this transition region, which is a few millimeters thick, the electron density decreases to a sufficiently small value that the ambipolar diffusion approximation is not valid and electrons diffuse freely. By taking the ambipolar limit, the diffusion rate of electrons in the transition region is smaller than might otherwise be calculated.

To verify that the ambipolar diffusion approximation did not prejudice the calculation by underestimating the diffusion of electrons at the edge of the arc, separate transport equations were written for electrons and ions. The radial electric field was then calculated by explicitly solving Poisson's equation. When free diffusion at the edge of the arc was allowed, the arc was found to expand only a few percent faster but ultimately to the same filling fraction when compared to a similar calculation using the ambipolar approximation. Since the amount of computer time required for the formulation where Poisson's equation is solved was more than for the ambipolar approximation, all of the results discussed in this paper were obtained using the latter approximation.

The following differential equations were solved along each radial spoke in the sector space formulation:

$$\frac{\partial \rho}{\partial t} = -\frac{1}{r}\frac{\partial}{\partial r}(r\rho u) + \rho \frac{c_s}{d}\left(\frac{1}{P}\frac{\partial^2 P}{\partial \theta^2}\right)_k,$$ (2)

$$\frac{\partial n}{\partial t} = -\frac{1}{r}\frac{\partial}{\partial r}\left(r(u + \mu_I \xi)n + D_I \frac{\partial n}{\partial r}\right) + \sum_j n r_j' N_j - \sum_{i,j} n^{\alpha_{ij}} r_{ij}' N_i,$$ (3)

$$\frac{\partial}{\partial t}\left(\tfrac{3}{2}nkT_e\right) = \frac{ne^2 E^2}{m\sum_i \nu_{ci}} - \tfrac{3}{2}nk(T_e - T_g)\sum_i \nu_{ci}\left(\frac{2m}{M_i}\right)$$

$$+ \sum_{i,j} \tfrac{3}{2}kT_e n^{\alpha_{ij}} r_{ij}' N_i - n\left(\sum_{i<j}\epsilon_{ij} r_{ij} N_i - \sum_{i>j}\epsilon_{ij} r_{ij} N_i + \sum_j r_j' N_j(\epsilon_j' + \tfrac{3}{2}kT_e)\right) + \frac{1}{r}\frac{\partial}{\partial r}\left(r\lambda_e \frac{\partial T_e}{\partial r}\right),$$ (4)

$$\frac{\partial(\rho c_p T_g)}{\partial t} = -\frac{1}{r}\frac{\partial}{\partial r}(\rho c_p T_g u) + \tfrac{3}{2}nk(T_e - T_g)\sum_i \nu_{ci}\left(\frac{2m}{M_i}\right) + \frac{1}{r}\frac{\partial}{\partial r}\left(r\lambda_g \frac{\partial T_g}{\partial r}\right),$$ (5)

$$\frac{\partial(\rho u)}{\partial t} = -\frac{1}{r}\frac{\partial}{\partial r}(r\rho u^2) - \frac{\partial P}{\partial r} + \frac{1}{r}\frac{\partial}{\partial r}\left[r\nu\left(2\frac{\partial u}{\partial r} - \frac{2}{3}\frac{1}{r}\frac{\partial}{\partial r}(ru)\right)\right].$$ (6)

Equation (2) is simply the heavy particle continuity equation where ρ is the mass density and u is the convective velocity. The last term in Eq. (2) is the correction to ρ in the kth sector for azimuthal convection. The azimuthal coordinate is θ, the tube diameter is d, and c_s is the sound speed.

Equation (3) is the charged particle continuity equation where μ_I is the ion mobility, ξ is the radial ambipolar electric field, D_I is the ion diffusion constant, r_j' is the electron impact ionization rate for species N_j, and r_{ij}' is the ion recombination coefficient for species i by process j. The forces re-

sulting from self-generated magnetic fields are incorporated into the radial ambipolar electric field in a manner described below. In Eq. (4), the electron energy equation, E is the longitudinal electric field, m and M_i are the electron and heavy particle masses, ν_{ci} is the electron momentum transfer collision frequency with species i, r_{ij} is the rate of electron impact excitation or relaxation between levels i and j of xenon with energy separation ϵ_{ij} and λ_e is the electron thermal conductivity. ϵ_j^i is the ionization potential of species j. Heavy particle energy conservation is described by Equation (5) where c_p is the heavy particle heat capacity, and λ_g is the heavy particle thermal conductivity.[22] Momentum conservation is given by Eq. (6) where P is the thermodynamic pressure, and ν is the viscosity.[22,23]

For the flashlamps of interest (filling pressures of a few hundred Torr and diameters in excess of 1 cm) the time required for the plasma to fill the bore is tens to hundreds of microseconds.[18,24,25] This is also the hydrodynamic timescale, the time required for the gas to convectively move and hence the time required for the gas density to change locally. We assume that the electrical input energy is significantly less than the single shot explosion energy of the flashlamp, and hence we are in a regime where strong shock waves are not likely to occur. The electron temperature and density change locally on a somewhat smaller time scale, microseconds to tens of microseconds. This time, though, is still long compared to the time required for excited states of the xenon atom to come into equilibrium with the local electron temperature and density, and heavy particle density. This equilibration time is typically less than a microsecond. In the model, we therefore made the assumption that the excited states of xenon, as well as that of the molecular xenon ion, are in equilibrium with the above mentioned quantities. The densities of the excited states and molecular ions were obtained by setting the derivatives of the appropriate rate
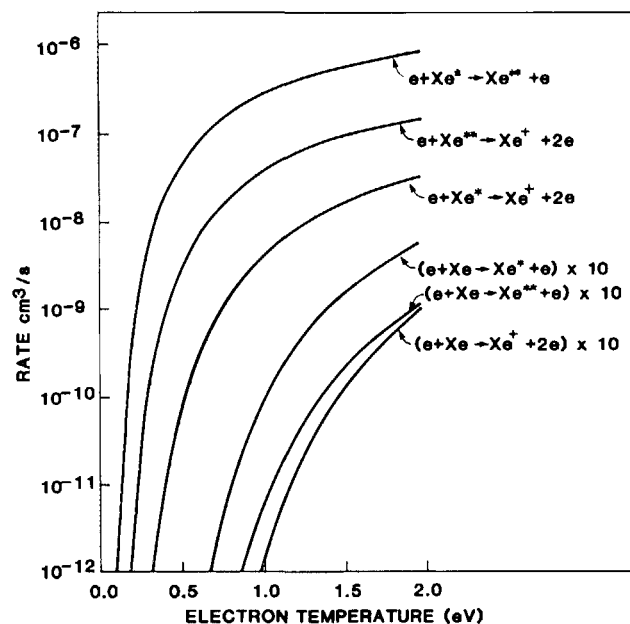

FIG. 3. Electron impact excitation rates for collisions with atomic xenon. Note that the rates for collisions with ground state xenon are multiplied by ten. The electron temperature is typically about 1.0 eV after the arc has expanded to its maximum extent.

equations equal to zero and solving for the quasi-steady-state values.

Two lumped excited states of xenon were included in the model. The excitation energy of these pseudo states and the approximate corresponding actual states of the xenon atom are 8.3 eV ($6s$) and 9.7 eV ($6p,5d,6s$). The rate equations that were solved to obtain the quasi-steady-state densities of these pseudostates, and those of the molecular xenon ion are written below. The ground state of xenon is denoted by Xe (level 0), the first excited state by Xe* (level 1) and the second excited state by Xe** (level 2). The atomic ion, Xe$^+$, is level I.

$$\frac{\partial [Xe^*]}{\partial t} = n_e \left[[Xe]r_{01} + [Xe^{**}]r_{21} - [Xe^*](r_{10} + r_{12} + r_{1I}) \right]$$

$$- [Xe^*]\left(\frac{1}{\tau_{10}} + \frac{1}{\tau_c} \right) + [[Xe^*] + [Xe^{**}]] (r_p + r_{ae} + M^2 r_a), \tag{7}$$

$$\frac{\partial [Xe^{**}]}{\partial t} = n_e \left[[Xe]r_{02} + [Xe^*]r_{12} - [Xe^{**}](r_{20} + r_{21} + r_{2I}) + [Xe_2^+]r_d + [Xe^+](r_r + n_e r_{cr}) \right]$$

$$- [Xe^{**}]\left(\frac{1}{\tau_{20}} + \frac{1}{\tau_{21}} + \frac{1}{\tau_c} + ([Xe^*] + [Xe^{**}])(r_p + r_{ae}) + M^2 r_a \right) + [Xe^{**}]\frac{1}{\tau_{21}}, \tag{8}$$

$$\frac{\partial [Xe_2^+]}{\partial t} = [Xe^+]M^2 r_{aI} + [Xe_2^*]^2 r_{ae} - [Xe_2^+]n_e r_d, \tag{9}$$

$$\frac{\partial [Xe_2^*]}{\partial t} = [[Xe^*] + [Xe^{**}]]M^2 r_a - [Xe_2^*]\left(Mr_N + n_e r_e + [Xe_2^*]r_{ae} + \frac{1}{\tau_r} \right) \tag{10}$$

The ratio of the density of the molecular ion to that of the total ion density is

$$\frac{[Xe_2^+]}{[Xe^+] + [Xe_2^+]} = \frac{n_e M^2 r_{aI} + [Xe_2^*]^2 r_{ae}}{n_e(n_e r_d + M^2 r_{aI})}. \tag{11}$$

For our typical values, this ratio is approximately 10^{-4}. The atomic ion and heavy particle densities are obtained by solv-

ing the partial differential Eqs. (2)–(6) discussed above. In Eqs. (7)–(11), M is any third body, r_{ij} is the rate of electron impact excitation between levels i and j, r_{iI} is the electron impact ionization rate for state i, r_r is the rate of radiative electron-ion recombination, r_{cr} is the rate of collisional radiative recombination, and r_a is the rate of formation of Xe$_2^*$ from collisions between excited xenon atoms and third bo-

TABLE I. Electron impact and heavy particle collision rates.

Symbol	Process	Rate[a]	Reference
r_p	Xe* + Xe* → Xe+ + Xe + e	5(−10)	33, c)
r_{ae}	Xe*_2 + Xe*_2 → Xe_2+ + 2Xe + e	5(−10)	33, c)
r_a	Xe** + Xe + M → Xe*_2 + M	1(−31) cm^6 s^{-1}	33, c)
r_r	e + Xe+ → Xe + hv	6.4(−13)/$T_e^{1/2}$	29, d)
r_{cr}	2e + Xe+ → Xe + e	5.1(−27)/$T_e^{4.5}$ cm^6 s^{-1}	29,35, d)
r_{al}	Xe+ + Xe + M → Xe_2+ + M	2.5(−31) cm^6 s^{-1}	33, c)
r_N	Xe*_2 + M → 2Xe + M	1(−11)	33, c)
r_e	Xe*_2 + e → 2Xe + e	1(−9)	33
r_d	Xe_2+ + e → Xe** + Xe	2.5(−7)·[1 − exp(−750/T_g)]/$T_e^{1/2}$	33,34, d)
$1/\tau_{21}$	Xe** → Xe* + hv	5(7) s^{-1}	estimate
$1/\tau_c$	Xe** + M → Xe* + M	3(−12)	estimate, c), e)
$1/\tau_r$	Xe*_2 → 2Xe + hv	2(7) s^{-1}	36, f)
$1/\tau_{10}$	Xe* → Xe + hv	1(4) s^{-1}	estimate, g)
$1/\tau_{20}$	Xe** → Xe + hv	5(7) s^{-1}	estimate, g)
r_{01}	e + Xe ⇌ Xe* + e	b)	37
r_{02}	e + Xe ⇌ Xe** + e	b)	37
r_{0I}	e + Xe → Xe+ + 2e	b)	38
r_{12}	e + Xe* ⇌ Xe** + e	b)	37,39
r_{1I}	e + Xe* → Xe+ + 2e	b)	40
r_{2I}	e + Xe** → Xe+ + 2e	b)	40,41
$v_c/[Xe]$	e + Xe → Xe + e	b)	42, h)
$v_{cI}/[Xe^+]$	e + Xe+ → Xe+ + e	2.9(−6) ln Λ /$T_e^{3/2}$	20, d), i)

a) 5(−7)≡5×10^{-7}. Rates are in units of cm^3 s^{-1} unless noted otherwise.

b) Cross section for process, from the indicated reference, was averaged over a Maxwellian electron distribution function to obtain rates as a function of electron temperature. Rates are plotted in Fig. 3. Reverse rates were calculated by detailed balance.

c) All rates for heavy particle collisions are listed for T_g = 300 °K. Rates were scaled in the model by $(T_g/300 °K)^{1/2}$.

d) T_g in °K, T_e in eV.

e) Applicable for quenching of excited states to any lower level.

f) Estimated average value, predominantly for triplet.

g) Estimated values for radiatively trapped transition.

h) Applicable for a neutral atomic xenon species.

i) $A = 1.55(10)(T_e^{3/2}/n_e)^{1/2}$; T_e in eV, n_e in cm^{-3}.

dies. The rate of formation of the molecular xenon ion through the neutral channel is r_{ae} and through the ion channel is r_{al}. r_d is the rate of dissociative recombination of the molecular xenon ion. Radiative lifetimes are denoted by τ_{ij} or τ_r, and collisional lifetimes by τ_c. The electron impact rates are plotted in Fig. 3. Heavy particle rates and lifetimes are listed in Table I.

C. Boundary conditions and thermal conduction

The boundary condition for transport equations in geometries with radial symmetry is that spatial gradients are zero at the center of symmetry. This is not the case for the sector space formulation. The length of the radius vector 180° opposed to a given sector is not necessarily the same length, and therefore the rate of expansion along that sector may not be the same as its opposing neighbor. Spatial derivatives must therefore be explicitly calculated across the center of symmetry. The only explicit boundary condition at the center of symmetry is that the value for a given variable for all sectors be equal. The boundary conditions at the opposite end of the sector, that is at the wall, are $T_g = T_w$, $u = 0$, and $n = 0$ where T_w is the wall temperature, calculated in the manner described below.

The boundary condition for the electron temperature at the wall is that $\nabla \cdot (\lambda_e \nabla T_e) = 0$. This boundary condition becomes evident when one examines the sheath that exists at the wall of the discharge tube. The sheath is a region in which the electron density decreases rapidly. Since the electron thermal conductivity is proportional to the electron density,[20] the rate at which heat is conducted by electrons through the sheath is negligible. The thickness of the sheath is a few to about ten Debye lengths,[20] which is only a few tens of microns for our conditions and which is much smaller than the grid spacing used in the calculation (typically a few tenths of a millimeter). Structure in the sheath is therefore not resolved, and as an approximation, we use the boundary condition described above. In practice, the contribution of electron thermal conduction to the electron energy balance is small during the discharge pulse.

The average wall temperature of a xenon flashlamp will increase by a few degrees many seconds after a single discharge pulse. Due to the short duration of the discharge pulse and low thermal conductivity of the quartz discharge tube, though, the inner surface of the quartz envelope can be heated many hundreds of degrees during the course of the discharge pulse. The inside surface of the quartz envelope is heated primarily by three sources; the thermal contribution of the electron and ion flux flowing to the wall, the energy released when electrons and ions diffusing to the walls recombine, and radiation emitted by the plasma that is absorbed in the walls. Of these three mechanisms, the domi-

nant source of wall heating is by recombination at the wall.[26,27] The thickness of wall material in which this energy is deposited in is $\Delta l \approx (\gamma \Delta t)^{1/2}$ where Δl is the heated thickness, Δt is the discharge pulse length, and γ is the thermal diffusivity of the wall. For typical values, $(\Delta t = 500 \mu s, \gamma = 8 \times 10^{-3} cm^2/s)$, the heated thickness is approximately 20 μm. Given this value, the inside surface wall temperature, T_w, at the terminus of each sector in the model is given by

$$\frac{\partial T_w}{\partial t} = \frac{1}{(\Delta l c_p)} \left(F_H - \frac{\lambda}{\Delta l} T_w \right) \quad (12)$$

where c_p is the heat capacity and λ is the thermal conductivity of quartz. The heat flux, F_H is[26,27]

$$F_H = \frac{n}{4} \left[v_I(\tfrac{3}{2}kT_I + E_I - e\phi_s) + \tfrac{3}{2}v_e kT_e e^{kT_e/e\phi_s} \right]. \quad (13)$$

In Eq. (13), v_I and v_e are the ion and electron thermal velocities, T_I and T_e are the ion and electron temperatures, n is the electron and ion density in the plasma adjacent to the sheath, ϕ_s is the sheath potential, and E_I is the xenon ionization potential. The sheath potential is given by[20]

$$\phi_s = -\frac{kT_e}{2e} \ln[MT_e/(mT_I)], \quad (14)$$

where M and m are the ion and electron masses, respectively. A separate wall temperature is computed for the terminus of each sector. This value becomes the boundary condition for the gas temperature at that location.

D. Magnetic forces and radial electric field

The magnetic forces generated by a high current arc or discharge may be sufficiently large to perturb the plasma. This force is the mechanism which compresses "pinch" plasmas. The origin of the force is that the current generates a magnetic field described by Maxwell's equation

$$\nabla \times \mathbf{B} = \frac{1}{c^2}\frac{\partial \mathbf{E}}{\partial t} + \mu_0 \mathbf{j}. \quad (15)$$

The magnetic field in turn induces a force on the charge carriers

$$\mathbf{F} = e\mathbf{j} \times \mathbf{B}. \quad (16)$$

For our geometry, this is a radial force pointing towards the axis or center of symmetry. For the conditions typical of xenon flashlamps the transport of charge carriers is collisionally dominated and the transverse motion of electrons and ions is dictated by ambipolar diffusion. For these conditions, the radial force resulting from the arc's magnetic field can be expressed as an effective drift velocity. This drift velocity, and the associated flux, is then used in the calculation of the effective radial ambipolar electric field. The magnetic field at radius r from the center of symmetry is

$$B = \frac{\mu_0}{2\pi} \int_0^r \sigma(r')\frac{E(r')dA'}{r'}, \quad (17)$$

where σ is the electrical conductivity, E is the longitudinal electric field, and the current density is $j = \sigma E$. The magnetic force at radius r is therefore

$$F_m = \frac{\mu_0 \sigma^2(r)E(r)}{2\pi} \int_0^r \frac{\sigma(r')E(r')dA'}{r'}. \quad (18)$$

Assuming quasi-steady-state conditions, the magnetic drift velocity is v_m where

$$\frac{dv_m}{dt} = \frac{F_m}{M} - v_c v_m = 0, \quad (19)$$

where v_c is the electron or ion collision frequency and M is the particle mass. Substituting for F_m, the magnetic drift velocity is

$$v_m = \frac{\mu_0 \sigma^2 E^2 M}{v_c} \int_0^r \frac{\sigma(r')dA'}{r'}, \quad (20)$$

where the electrical conductivity is en/mv_c and the longitudinal electric field is independent of r. The effective radial electric field is obtained by setting the radial flux of electrons equal to that of ions. This is the ambipolar diffusion approximation. For our conditions, diffusive motion is a second order correction to the convective motion of the heavy particles. Solving for the radial electric field,

$$\xi = \left[-(u_e + v_{m_e}) + (U_I + v_{m_I}) \right.$$
$$\left. + (D_e - D_I)\nabla n/n \right]/(\mu_e + \mu_I) \quad (21)$$

where u is the convective velocity, μ is the particle mobility, D is the free diffusion coefficient and the subscripts e and i refer to electrons and ions. The magnetic drift velocity is only important at low pressure (< 100 Torr) and high current density (> 3000 A/cm^2). This effect results from the fact that the magnetic drift velocity is proportional to the third power of the mobility, which is in turn inversely proportional to the pressure.

E. External circuit

The external circuit used to drive the flashlamp is shown in Fig. 4. The storage capacitance is C_s and the cable (or peaking) capacitance is C_p. A series resistance of R_s may also be in the circuit. The circuit equations used in the model are (see Fig. 4 for notation)

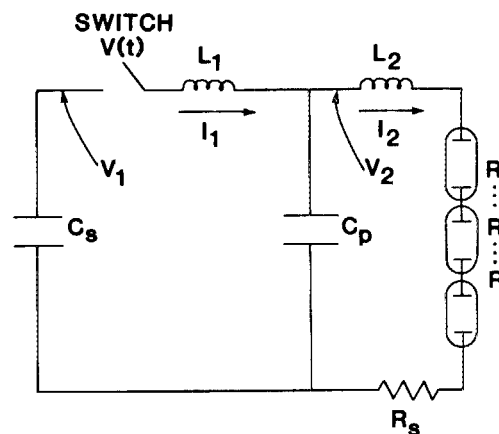$$\frac{dV_1}{dt} = -\frac{-I_1}{C_s} + V(t), \quad \frac{dV_2}{dt} = \frac{I_1 - I_2}{C_p}, \quad (22)$$

FIG. 4. Discharge circuit used in the model. C_s is the storage capacitor and C_p is a peaking capacitance, either in the electrical cables or added to the circuit. The inductance L_1 is added to the circuit to obtain the desired LC time constant for the circuit length and the inductance L_2 is geometrical. Each lamp has a resistance R and R_s is a series resistance.

$$\frac{dI_1}{dt} = \frac{V_1 - V_2}{L_1}, \quad \frac{dI_2}{dt} = \frac{V_2 - I_2(nR + R_s)}{L_2}, \quad (23)$$

where n is the number of lamps in series in the circuit and R is the resistance of each lamp. This last value is given by Eq. (1) for every sector, and each sector is treated as one in a set of parallel resistors. The function $V(t)$ simulates the circuit switching device (e.g., a spark gap or a thyratron). The final results from the model are insensitive to the precise form of this function since the time required for the circuit switching device to conduct is very short compared to any other time of interest and is independent of other circuit parameters. $V(t)$ is approximated by

$$V(t) = \frac{V_0 e^{-t/\tau}}{\tau}, \quad (24)$$

where V_0 is the charging voltage and τ is the switching time ($\tau \approx 10$ ns).

F. Radiation transport

During the first few hundred microseconds of the discharge pulse of a xenon flashlamp having our dimensions and conditions of interest, the emission spectrum is initially dominated by line emission. After the first few hundred microseconds, the spectrum is dominated by continuum emission.[4,9,16] Line emission decreases in apparent magnitude in part due to increased Stark broadening by an increasing density of electrons. The continuous emission is otherwise dominated by radiation from electrons making free-bound recombination transitions.[9,28] The transformation from line to continuous emission occurs as the plasma within the arc approaches LTE conditions, and as the arc grows to sufficiently large size that the emissitivity of the plasma is large. Recall that continuous emission at frequency ν from a grey body at temperature T is $S(T,\nu)\epsilon(T,\nu)$ where $S(T,\nu)$ is the Planck blackbody emission function and $\epsilon(T,\nu)$ is the emissivity of the source, equal to unity for a black body. The emmissivity of a cylindrical plasma with diameter d and absorption coefficient $\alpha(T,\nu)$ can be approximated by[24]

$$\epsilon \approx 1 - \exp\left(\frac{-\alpha d}{[1 + 0.7(\alpha d)^{1/2} + 0.08\alpha d]}\right). \quad (25)$$

For spectral emission mimicking that of a blackbody, the product αd must be large. Since α is relatively constant as a function of position within the arc, the emissivity of the plasma increases as the arc expands only as d increases. The emissivity of xenon arcs is a function of wavelength because α is a function of wavelength. α and ϵ are large in the visible and infrared, and small in the ultraviolet. This disparity in emissivity is manifested in the angular distribution of radiation from a flashlamp (see Sec. III D).

Radiation transport in this model was computed for only the continuum component of the spectrum, although line radiation (i.e., spontaneous emission) as an energy loss mechanism is included in the kinetics portion of the model. The local source of continuous radiation was assumed to be free-bound electron transitions. The radiation source function (photons/cm^3 $-$ s) is obtained by summing the radiative contributions from electrons making free-bound transitions (radiative recombination) to the ground and excited states of neutral xenon. The source function for photons having energy between ϵ_i and ϵ_i' resulting from radiative recombination of electrons with temperature T_e into a neutral xenon level with ionization potential E_k is[20]

$$S_{ik} = \gamma n^2 \int_{\frac{2}{m}(\epsilon_i - E_k)}^{\frac{2}{m}(\epsilon_i' - E_k)} \frac{\exp\left(\frac{-mx}{2kT_e}\right)}{\left(\frac{2E_k}{m} + x\right)} dx, \quad (26)$$

where γ is a normalization constant (see below). For use in the model, photons were grouped into five bins for the purpose of generating a coarse spectrum. The upper boundaries, in wavelength, of the first four photon groups are 0.104, 0.345, 0.564, and 5 μm. The fifth photon group comprises photons with wavelengths longer than 5 μm. The first three boundaries correspond to the threshold for ionization of the three neutral states of xenon used in the model, assuming a fixed lowering of the ionization potential of 0.2 eV. The normalization constant γ is chosen such that the sum of S_{ik} over the five photon groups and three neutral levels equals the rate of radiative recombination.[29] That is,

$$\sum_{i=1}^{5} \sum_{k=1}^{3} \frac{S_{ik}}{n^2} = \frac{6.4 \times 10^{-13}}{T_e^{1/2}}. \quad (27)$$

The electron temperature is in electron volts. Contributions are obtained only if $\epsilon_i > E_k$. The source function for group i is simply

$$S_i = \sum_{k=1}^{3} S_{ik}. \quad (28)$$

Given the source function for photon group i at location $\mathbf{r}$, $S_i(\mathbf{r})$, the local photon flux, $\Phi_i(\mathbf{r})$ is obtained by computing the photon transport integral

$$\Phi_i(\mathbf{r}) = \int_{S_i(\mathbf{r}')} \frac{\exp\left[-\int_{\mathbf{r}'}^{\mathbf{r}} \alpha_i(\mathbf{r}'') d|\mathbf{r}'' - \mathbf{r}'|\right]}{4\pi|\mathbf{r}'' - \mathbf{r}'|^2} d^3r', \quad (29)$$

where $\alpha_i(\mathbf{r})$ is the photon absorption coefficient. The photon absorption coefficient is the sum of a photoionization term and a term for inverse Bremsstrahlung. The first term was calculated by assuming hydrogenic bound-free photoionization of all neutral levels.[20] This photoionization cross section is maximum at threshold and decreases with the third power of the energy defect. The average absorption coefficient (cm^{-1}) by this process for photon group i is

$$\alpha_i^P = \sum_k \sum_{\epsilon_k < \epsilon_i} N_k \frac{7.9 \times 10^{-18}}{(\epsilon_i' - \epsilon_i)} \int_{\epsilon_i}^{\epsilon_i'} \frac{d\epsilon}{(\epsilon/E_k)^3}, \quad (30)$$

where N_k is the density of atoms in level k. Photon absorption by free-free absorption, small in comparison to photoionization, is given by[20]

$$\alpha_i^{FF} = 2.3 \times 10^4 [\text{Xe}^+] n \left(\frac{\pi m}{8kT_e}\right)^{1/2} \nu^{-3} \text{ cm}^{-1}. \quad (31)$$

Given the local photon flux, the rate of photoionization of level k at $\mathbf{r}$ is then

$$R_k(\mathbf{r}) = \sum_{\epsilon_i > E_k} \Phi_i(\mathbf{r}) \alpha_i^P(\mathbf{r}) N_k(\mathbf{r}). \quad (32)$$

For conditions where $\alpha_i(\mathbf{r})$ and $S_i(\mathbf{r})$ are constants and

the arc is radially symmetric, the integral in Eq. (29) can be performed in closed form. For our conditions, though, this is not the case. The integral in Eq. (29) was numerically evaluated in the model using time dependent local values for the source function and absorption coefficient. To save computer time, the integrals for $\Phi_i(\mathbf{r})$ were evaluated for sources lying only within a distance corresponding to less than ten absorption lengths (including axial extent). The radiation transport integrals were also only evaluated at time intervals of about 2–5 μs. This time interval is short enough to capture any significant transient behavior, but long enough to minimize computer time.

III. THE RATE OF ARC EXPANSION AND PLASMA BORE FILLING

A. Hydrodynamic effects

Current density and heavy particle density during a typical sequence of arc formation are plotted in Fig. 5. The arc filling fraction is plotted in Fig. 6. The discharge conditions are a xenon filling pressure of 300 Torr, a tube diameter of 2.0 cm and an arc length of 50 cm. Three lamps are in series in the electrical circuit and the charging voltage on the storage capacitor (312 μF) is 16.3 kV. The stored electrical energy in the circuit is 280 J/cm of arc length and the LC time constant of the electrical circuit is 265 μs. The arc was initiated midway between the axis and the wall of the discharge tube. Early in the discharge pulse, the arc diameter is small and the impedance of the discharge is large. Consequently, the local current density is large, though the total current is small. As the low gas density arc channel begins to form, the arc expands in a radially symmetric fashion. By 100 μs, the arc has reached the wall on one side of the discharge tube, but continues to expand on the other side. Nearly LTE conditions are obtained in the middle of the arc with the gas and electron temperatures ≈ 1.1 eV. (See Fig. 7.) At 250 μs, the convective motion of the gas has increased the gas density exterior to the arc to a sufficient degree as to stall the rate of arc expansion. For these pulsed conditions, the last frame in the sequence plotted in Fig. 5 is the maximum arc diameter, representing an arc filling fraction of 0.68. The slowing in the rate of arc expansion and its eventual stalling before the bore is filled is, to first order, a result of electron kinetic processes. The electron kinetic processes, though, are constrained by the heavy particle density determined by hydrodynamics. The hydrodynamics are, in turn, driven by a pressure gradient, which is a result of gas heating of heavy particles by electrons.

As the discharge develops, the gas entrained within the arc is heated, thereby raising the local pressure. The pressure gradient drives an expansion wave into the cool gas outside the arc, thereby increasing the gas density in that region. The electron temperature is proportional to E/N (electric field divided by gas density), and more specifically, is a function of E/ν (electric field divided by collision frequency). The decreasing gas density within the core of the arc and increasing density outside the core of the arc leads to a disparity in local electron temperature. The electron temperature is largest within the arc (because N is small) and decreases as the gas density increases towards the edge of the arc. This trend of

increasing electron temperature with decreasing radius into the arc continues until the ion density becomes sufficiently high that the collision frequency within the arc is dominated by electron-ion collisions. At this point, the electron temperature may then decrease within the arc. (See Fig. 7.)

As the arc channel expands, more gas is compressed by the expansion wave into a smaller region at the arc's edge. The parameter E/N, and hence electron temperature, continues to decrease. Recall that the ionization rate is proportional to $\exp(-\epsilon/T_e)$, where ϵ is the ionization potential, while the recombination rate is proportional to $1/T_e^n$ ($n = 0.7$ for radiative recombination, $n = 4.5$ for collisional radiative recombination).[29] The higher neutral gas density at the edge of the arc also increases the rate at which molecular xenon ions are formed, for which the recombination rate is more rapid than for atomic ions.[30] Therefore, as the gas density increases at the edge of the arc, the ionization rate decreases and the recombination rate increases. Eventually, the electron temperature falls below a critical value at which time the recombination rate dominates and the electrons are not energetic nor numerous enough to avalanche or to heat the gas at the edge of the arc. At this point, the arc expansion stalls. Further expansion takes place at a much reduced rate and by extension of the hot zone by heavy particle thermal conduction or by reversal in the direction of convection (see below). The reduction in electron temperature is exacerbated by a decrease in the impedance of the flashlamp as the arc channel expands. The lowered impedance results in a lower local electric field, and hence lower electron temperature. The lower electron temperature provides a smaller heat source, the driving function for the hydrodynamic pressure gradient.

The asymmetric expansion of the arc to the interior wall of the discharge tube results in asymmetric heating of that surface. The computed wall temperature at the interior surface of the discharge tube is plotted in Fig. 8, and reflects the asymmetric expansion of the arc. The dominant wall heating mechanism is the kinetic energy of ions accelerated through the sheath and recombination heating. Severe localized heating of the discharge tube is thought to be a failure mechanism when flashlamps are heavily electrically loaded. Thermal conduction within the discharge tube wall and throughout the volume of the glass, averages the azimuthal extent of the wall heating when measured on the outer surface of the wall. Even though, thermocouple measurements of the exterior wall temperature after a discharge pulse show a severe dependence on azimuthal position.[31] The measured temperature is highest at the wall location closest to the ground plane or trigger wire; at the azimuthal location one would expect the breakdown filament to be closest.

B. Electrical energy loading

The fact that the arc does not entirely fill the bore in large diameter flashlamps is a result of the transient nature of the excitation pulse. For sufficiently long electric discharge pulses, the extreme example being continuous excitation, diffusion and thermal conduction through the neutral gas will eventually heat the regions exterior to the arc channel. This is a much slower process than that of the initial

25 μs

0   0.25 0.50 0.75 1.0
           cm

50 μs

3000

A/cm² 2000

1000

0

100 μs

6×10¹⁹

4×10¹⁹

2×10¹⁹

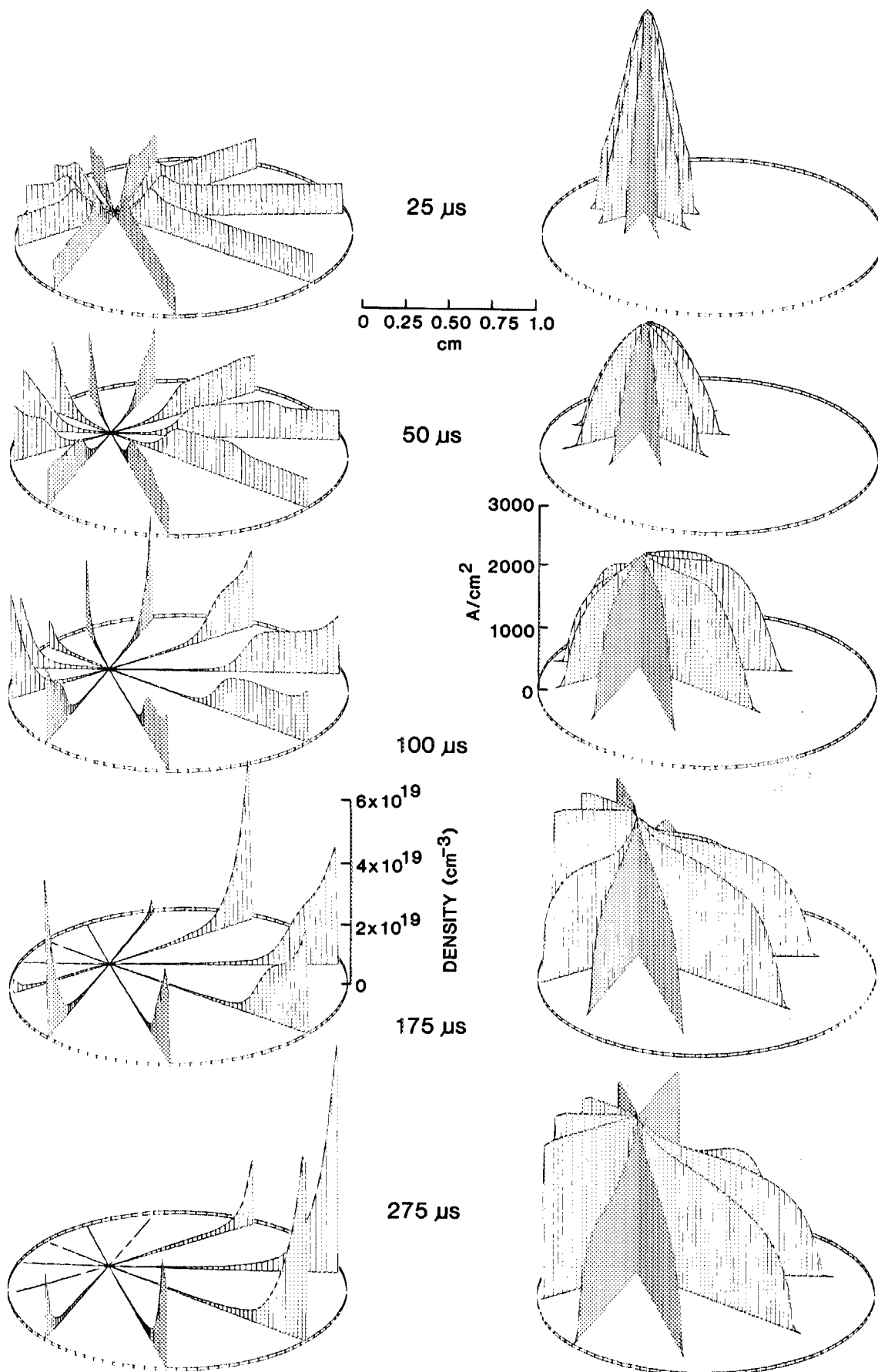0

DENSITY (cm⁻³)

175 μs

275 μs

FIG. 5. Typical sequence of arc expansion in a xenon flashlamp for various times after propagation of the breakdown filament. The initial conditions are an electron density of 10^{14} cm^{-3} confined to a diameter of 0.1 cm at the location of the filament. The gas density is initially quiescently uniform. The breakdown filament was located halfway between the axis and wall of the discharge. Plotted on the left is the neutral xenon density and on the right is the current density. The diameter of the discharge tube is 2.0 cm and the initial filling pressure is 300 Torr. A plot of the initial neutral gas density would appear as in Fig. 2, and initially there is no current density. The arc maintains the profiles as given for $t = 275$ μs for another 200 μs, yielding a bore filling fraction of 0.68.
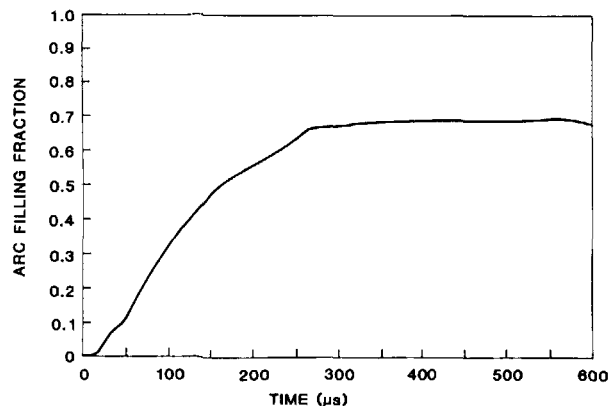
FIG. 6. Time history of the arc filling fraction corresponding to the conditions of Fig. 5. The arc filling fraction is defined as that fraction of the cross-sectional area of the tube in which the current density is greater than 0.1 of the instantaneous peak value of current density.

CIRCUMFERENTIAL POSITION

FIG. 8.Typical calculated interior wall temperature of the discharge tube at the end of the current pulse. Conditions are similar to those of Fig. 5. Wall heating is asymmetrical due to the initial breakdown filament being located off the axis of the discharge tube.

expansion mechanism. As the denser gas in the outer part of the arc heats up, the pressure gradient reverses, causing a net convection of gas back into the interior of the arc. This process continues until a steady-state temperature and density profile is obtained, the description of which is given by the standard steady-state heat transfer equations.

The eventual reversal of the pressure gradient and convection of gas back into the core can be observed on shorter time scales in flashlamps of relatively low pressure by increasing the electrical input energy to a sufficiently large value. An example of this process is shown in Fig. 9 where the heavy particle density for two values of electrical input energy are plotted. In each case, the arc was initiated on the axis of the tube. The discharge tube diameter is 5 cm and the initial fill pressure is 75 Torr. In Fig. 9(a) the electrical input energy in 70 J/cm; in Fig. 9(b) the input energy is 285 J/cm. In the former case, the input energy is sufficient to form the arc channel, however, it is sufficient to heat the gas exterior to the arc within the duration of the discharge pulse (hundreds of microseconds). In the latter case, the arc expands to fill the entire bore in about 250 μs. The denser gas in the outer portions of the arc is heated, thereby reversing the

pressure gradient and refilling the arc channel.

As implied above, the arc filling fraction is a function of energy loading of the lamp, and more accurately, a function of both energy deposited and the length of time for energy deposition. A discharge current pulse of time duration significantly less than the sound speed transit time across the discharge tube is not of sufficiently long duration to allow the arc channel to form by convective motion during the energy deposition phase. Conversely, the arc filling fraction for current pulses longer than the sound speed transit time is a function only of the stored electrical energy and energy deposited in the discharge. This dependence is illustrated in Fig. 10 where the arc filling fraction is plotted as a function of energy loading (tube diameter = 2.5 cm, filling pressure = 300 Torr). The arcs were initiated on the axis of the discharge tube. The arc filling fraction increases with increasing energy loading, rapidly at low loading and less rapidly at high loadings. This is also the experimentally observed behavior.[18,24] The roll off in arc filling fraction with larger energy loading is in part a result of radiation becoming a more efficient energy dissipation mechanism. The role of radiation in the arc expansion process is discussed in Sec. III D.

C. Pressure and geometrical effects

As described above, for otherwise identical conditions, the rate of arc expansion and arc filling fraction are functions of the electrical energy loading. They are also functions of the radius of the discharge tube, xenon filling pressure, and the radial location of the breakdown filament. Clearly, for otherwise identical conditions, the rate of arc expansion and final arc filling fraction increases with decreasing filling pressure.[18] (See Fig. 11.) For constant energy loading, the energy available per gas atom, and hence the largest possible arc temperature, increases with decreasing fill pressure. The
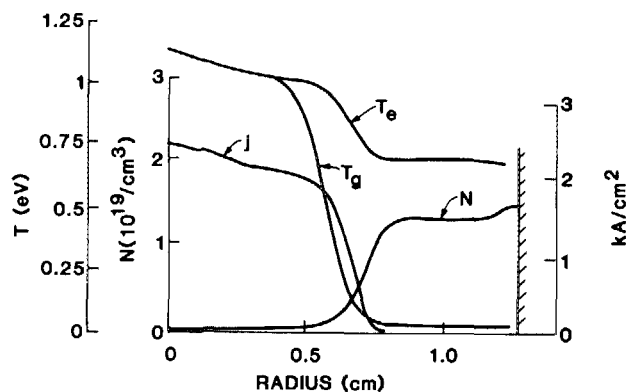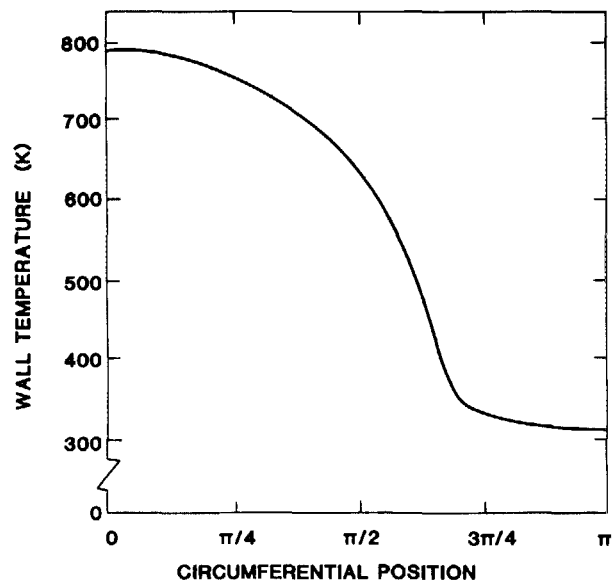

FIG. 7. Typical arc parameters for a symmetrical arc (i.e., the breakdown filament located at the center of the discharge tube). Conditions are plotted for $t = 90$ μs after breakdown, about halfway through the arc expansion process. The plasma is nearly in LTE in the core of the arc.
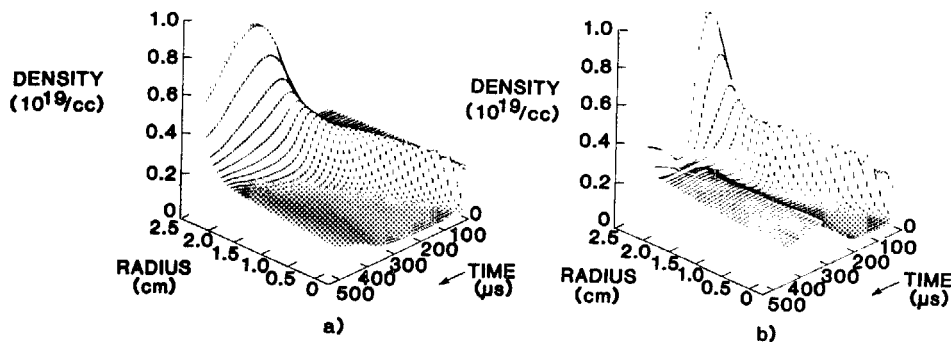
FIG. 9. Xenon density for two values of stored electrical energy per centimeter of arc length; (a) 70 J/cm and (b) 285 J/cm. The initial filling pressure is 75 Torr and the diameter of the discharge tube is 5 cm. The breakdown filament passes through the center of the tube.

increase in temperature in the core of the arc, though, is small (1.1 eV at 300 Torr and 0.9 eV at 400 Torr). The increase in filling fraction with decreasing gas pressure is a result of an increasing E/N at the edge of the arc. When the arc channel forms, a region of high gas density at the edge of the arc is created by convection. It is the lowered value of E/N at the edge of the arc that has major responsibility for stalling the arc expansion process. At lower fill pressure, the arc can expand to a larger radius before the critically low E/N is obtained in the high gas density region at the edge of the arc.

The radial location of the breakdown filament at each axial point determines the bore filling fraction at that point. In general, the bore filling fraction is maximum when the breakdown filament is on the axis. The bore filling fraction decreases as the breakdown filament moves from the axis towards the wall. (See Fig. 12.) This effect is a function of xenon filling pressure, with high pressures being most sensitive to the location of the breakdown filament. To understand this phenomenon, think of the expansion wave propagating along each sector as having to displace a given amount of gas in order to form the low density arc channel.

Since the system is bounded, the displaced gas accumulates in front of the wave, thereby requiring a larger pressure gradient across the boundary to continue the expansion process. The amount of gas that must be displaced, and therefore accumulates in front of the expansion wave, is proportional to the square of the length of the sector. Breakdown filaments at off axis locations have sectors that are disproportionately long, and expansion along those sectors is slow, thereby accounting for a low filling fraction. (See Fig. 13.) This effect is also seen in the dependence of bore filling fraction on the diameter of the discharge tube. In Fig. 14, this dependence is plotted for breakdown filaments located on the axis of the discharge tube. The volumetric power loading is the same for all cases. The bore filling fraction decreases as the diameter of the discharge tube increases, a manifestation of the effect discussed above.

D. Radiation and its role in arc dynamics

The internal energy of a plasma is calculated from the heavy particle temperature and density, lowering of the ionization potential, and the partition function of the constituents of the plasma. For the conditions of interest (filling pressure = 300 Torr, temperature ≈ 1 eV) the internal energy of a xenon plasma is approximately 6.5 J/cm³. The electrical energy deposited in the plasma, though, is usually much larger than this value. Typically, 95% of the stored electrical
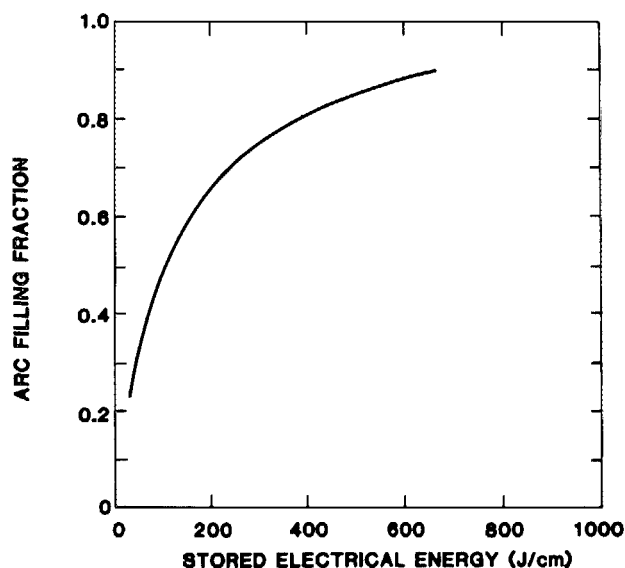

FIG. 10. Arc filling fraction as a function of stored electrical energy per centimeter of arc length. The discharge tube is 2.5 cm in diameter, arc length is 112 cm, and the initial xenon filling pressure is 300 Torr. Stored electrical energy was varied by changing the charging voltage on the storage capacitor ($C_t = 431\,\mu$F). The voltage corresponding to 250 J/cm is 11.4 kV.
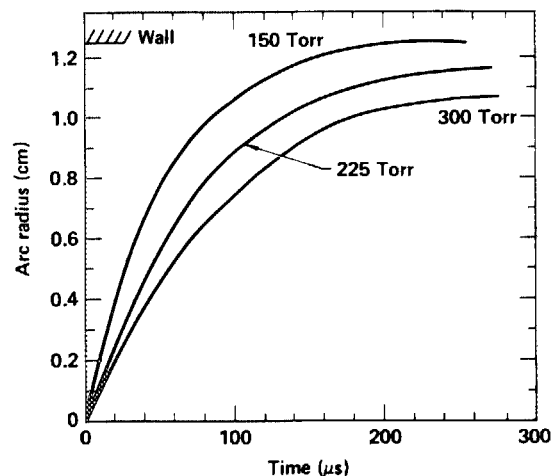

FIG. 11. Arc expansion for filaments located at the center of the discharge tube for different filling pressures of xenon. The discharge tube is 2.5 cm in diameter, and the stored electrical energy is 260 J/cm of arc length.
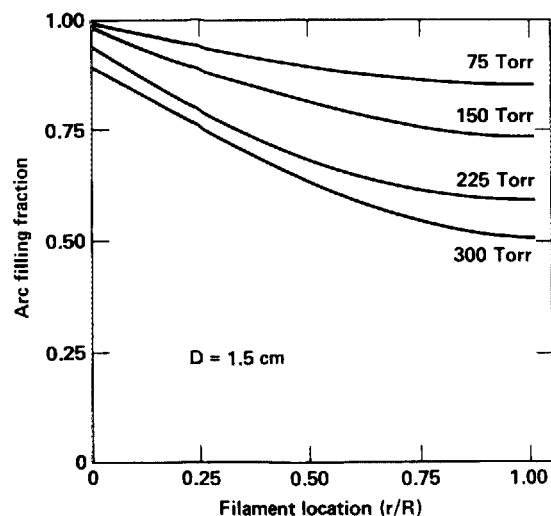
FIG. 12. Arc filling fraction as a function of filling pressure of xenon and location of the breakdown filament. A value of $r/R = 0$ corresponds to the breakdown filament being at the center of the discharge tube and a value of $r/R = 1$ corresponds to the filament running along the wall of the discharge tube. The diameter of the discharge tube is 1.5 cm and the stored electrical energy is 105 J/cm of arc length. The arc filling fraction decreases with increasing fill pressure and as the breakdown filament moves away from the axis of the tube and towards the wall.

cle density significantly less than the cross-sectional average. Therefore, the disparity between the internal energy of the plasma and the deposited electrical energy in the plasma is even larger than mentioned above.

The difference between energy deposited in the discharge tube and that energy which is stored as the internal energy of the plasma is the energy that is either deposited in the wall of the discharge tube or radiated away. The former is the smaller effect, accounting for less than 20% of the total energy.[31] The latter is the single greatest expenditure of energy in the plasma. Of the energy deposited in the plasma approximately 75% is eventually radiated away.[31] As the plasma in the interior of the arc obtains temperatures near 1 eV and conditions approach LTE, the emissivity of the plasma increases and the radiation process becomes quite efficient. Electrical energy deposited in the plasma and would otherwise be available for the thermodynamic expansion of the arc channel is radiated away instead, thereby contributing to the slowing down and eventual stalling of the arc expansion process.

The partitioning of deposited electrical energy into radiation and other processes in a xenon flashlamp is illustrated in Fig. 15. Here the total energy deposited in a xenon flashlamp, and the total energy radiated by the lamp are plotted as a function of time. The former plot was experimentally obtained by integrating the product of voltage and current of the flashlamp. The latter plot was experimentally obtained by integrating the signal from an energy calibrated pyroelectric detector. Also shown, by the horizontal line in Fig. 15, is the amount of energy that must be deposited in the plasma to raise the temperature of all the gas in the lamp to 1.1 eV. Clearly, the amount of energy deposited in the lamp is sufficient to heat the entire bore to a temperature in excess of 1.1 eV. The energy actually available to do so, though, is at best the difference between the energy deposited in the gas and the energy radiated away. This smaller amount of ener-

energy can be deposited in the discharge tube during a discharge pulse lasting 500 μs. This value corresponds to approximately 50 J/cm^3. It would appear that there is sufficient energy to raise all of the gas in the flashlamp to a temperature in excess of 1 eV, and therefore fill the entire bore with plasma. In reality, though, the internal energy of the plasma is even less than the value one would calculate using a heavy particle density given by the initial filling pressure because that portion of the bore that is filled with plasma and therefore at the high temperature, has a heavy parti-
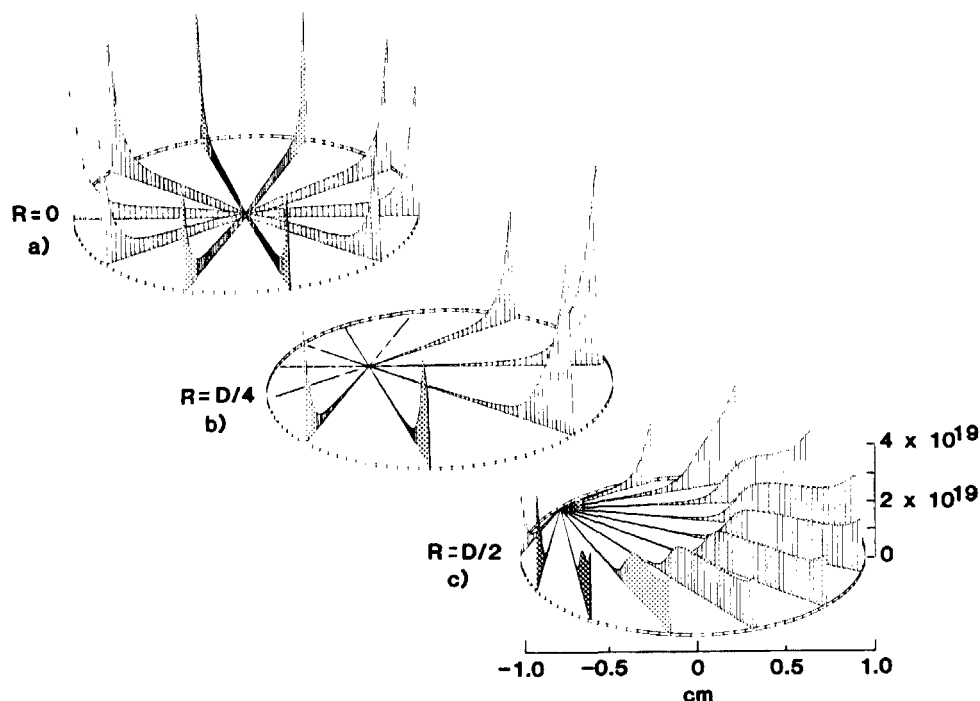

FIG. 13. Xenon density for fully developed arcs for different locations of the breakdown filament; (a) center of the discharge tube, (b) midway between axis and wall, and (c) along wall of the discharge tube. The discharge tubes are 2.0 cm in diameter and the initial filling pressure of xenon is 300 Torr. The stored electrical energy is 280 J/cm of arc length. The arc filling fractions are 0.85, 0.7, and 0.5, respectively.
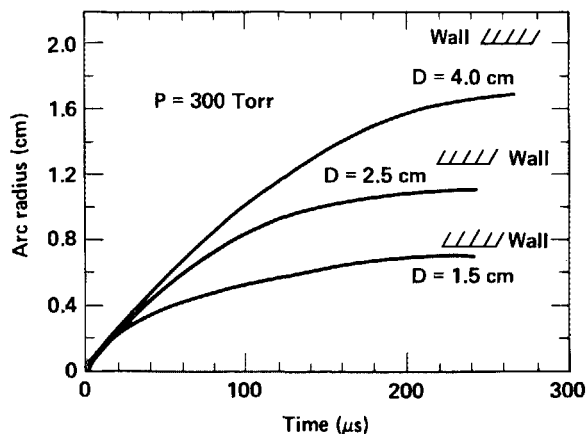
FIG. 14. Arc radius as a function of diameter of the discharge tube for an initial filling pressure of xenon of 300 Torr. The stored electrical energy in each case is 0.4 of the single-shot explosion energy. The stored electrical energy per cm of arc length (in increasing order of diameter) are 170, 420, and 965 J/cm.

gy is sufficient to raise only a portion of the gas to the desired temperature. The bore filling fraction therefore has as a maximum a value necessarily less than unity.

We see then that the slowing down in the rate of arc expansion and the eventual stalling of the arc expansion is in part a result of reaching a state in which energy is radiated away at a rate equal or comparable to the rate of energy deposition and therefore this energy is unavailable for the thermodynamic expansion of the arc. A system whose emissivity is lower, and hence is a poorer radiator of energy, has more internal energy available for the hydrodynamic expansion of the arc channel. One would expect larger arc channels and larger filling fractions for such systems.

Radiation inhibits the rate of arc expansion and reduces the arc filling fraction due to the fact that it is an efficient energy dissipation mechanism. To the extent that radiation is also a source of ionization, radiation transport increases the rate of arc expansion, but does not appreciably change the final arc filling fraction. Radiation serves to speed of the hydrodynamic timescale during the early stages of the discharge pulse when the applied electric field is high. While the field is high, photoelectrons created at the edge of the arc are

able to rapidly avalanche, thereby expanding the plasma region, heating the gas, and spatially extending the pressure gradient front. As the arc expands, arc impedance and applied voltage decrease, and the gas density increases at the edge of the arc. The electron temperature in this region drops below a value sufficient to allow photoelectrons to avalanche. The electron temperature, though, is above the value necessary to maintain the plasma. Photoionization still occurs at the edge of the arc at this time, however the photoelectrons are not hot enough to expand the arc channel to a larger diameter.

The extent to which radiation increases the rate of arc expansion is illustrated in Fig. 16 where arc radius as a function of time is plotted for calculations with and without photoionization. The example with photoionization expands more quickly however the ultimate filling fraction is the same as the otherwise identical example without photoionization.

Recall that the emissivity of a plasma is an exponential function of the optical depth of the plasma. [See Eq. (25).] The optical depth, the product of the absorption coefficient and the photon's path length, is a function of the angle of observation. At shallow angles, the photons one observes have, on the average, traversed a longer length of plasma than have photons that are observed at right angles to the axis of the plasma. As the arc channel expands, the path that is traversed by photons observed at various angles lengthens. Since the photon absorption coefficient is a function of wavelength, the change in path length as a function of time and angle of observation requires that the observed spectrum is also a function of these values.

The angular dependence of the emission spectrum can be directly calculated with our flashlamp model. With the time and spatially dependent photon source terms and absorption coefficients generated by the model, one simply computes the radiation transport integral [Eq. (29)] at a location on the surface of the discharge tube for photons arriving in a given cone angle. Doing so, we plotted in Fig. 17 the ratio
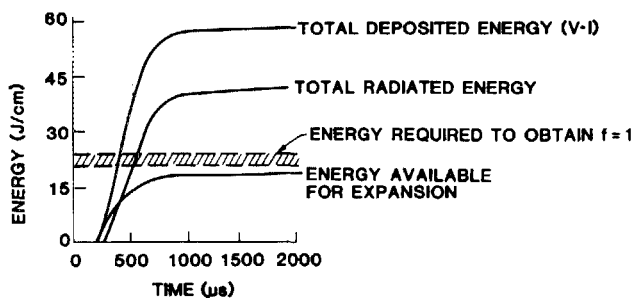

FIG. 15. Experimental data taken on a xenon flashlamp 1.9 cm in diameter and having an initial xenon filling pressure of 300 Torr. The total energy deposited in the discharge tube and the total radiated energy per cm of arc length are plotted. The energy available for the thermodynamic expansion of the arc is at best the difference between the two values. The banded region is the approximate energy required to obtain an arc filling fraction of unity with a temperature of 1.1 eV.
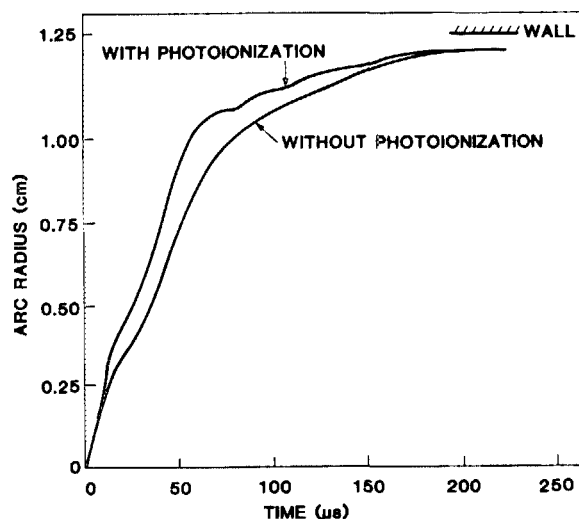

FIG. 16. Arc radius in a discharge tube 2.5 cm in diameter with and without photoionization. Radiation, as an energy loss mechanism, is included in both calculations.
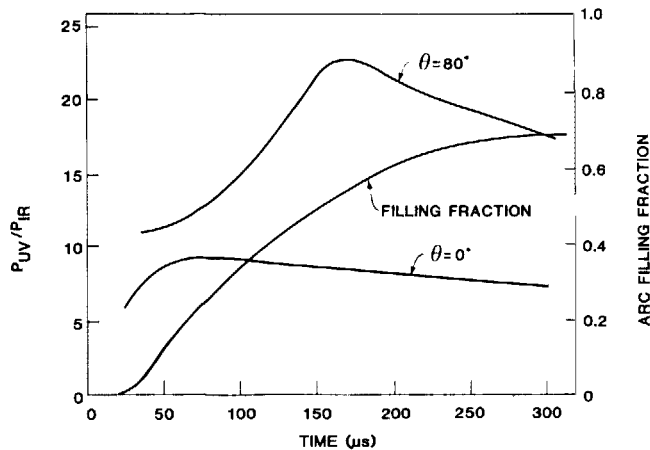
FIG. 17. Ratios of radiated power for two angles of observation and arc filling fraction, for a discharge tube 1.9 cm in diameter. The angles are for viewing the lamp perpendicular to the axis $(\theta = 0°)$ and for viewing at a grazing incidence to the tube $(\theta = 80°)$. The plotted ratio is of power radiated at UV wavelengths $(\lambda < 0.345 \mu m)$ divided by power radiated at IR wavelengths $(\lambda > 1.0 \mu m)$. Parallel lines for these ratios would indicate that the additional path length, and hence absorption, that photons experience as the arc expands has the same effect for all wavelengths. The dramatic increase in the ratio for the grazing incidence as compared to the normal incidence results from the UV photons having a smaller absorption coefficient.

of power radiated in the ultraviolet $(\lambda < 0.345 \mu m)$ to that radiated in the infrared $(\lambda > 1 \mu m)$ for angles of observation of 0° (perpendicular) and 80° (nearly grazing), and as a function of time.

Recall that the absorption coefficient is large for the infrared and small for the ultraviolet. At early times, the arc radius is small and optical depth for all photons is small. At later times when the arc radius is larger, the optical depth for the infrared is large, while that for the ultraviolet, increasing by the same fraction, on an absolute scale remains fairly small. At normal incidence, the absolute difference in the absorption coefficient between the IR and UV does not increase sufficiently for the ratio of radiated powers to change significantly. At shallow angles, though, the photons traverse a longer path through the plasma as the arc radius increases. The absolute change in optical depth between the IR and the UV becomes sufficiently large that the IR is absorbed relative to the UV. The ratio of power radiated in the UV as compared to the IR therefore increases.[32]

IV. CONCLUDING REMARKS

A model for xenon flashlamps has been discussed that, from first principles, describes the arc formation process. This model, using a pseudo two-spatial-dimension formulation, shows that the arc filling fraction is a function of the radial location of the breakdown filament, as well as of the filling pressure, energy loading and diameter of the discharge tube. The arc filling fraction is largest for arcs initiated on the axis, and decreases as the breakdown filament moves off the axis toward the wall. The slowing and termination of the arc expansion process at filling fractions less than unity results from a decrease in E/N in the high-density gas exterior to the arc and from the efficient conversion, and subsequent recombination, of atomic xenon ions to molecu-

lar xenon ions. Radiation serves primarily to reduce the rate of arc expansion by efficiently converting thermal energy in the plasma to photons that escape from the system. The increase in arc radius is manifested in the change in spectral content of radiation observed as a function of angle. Photon absorption coefficients are larger in the IR than in the UV. Therefore when observed at shallow angles as the arc expands, the emission spectrum is increasingly blue shifted.

[1]J. H. Goncz, J. Appl. Phys. **36**, 742 (1965).
[2]J. P. Markiewicz and J. L. Emmett, IEEE J. Quantum Electron. QE-2, 707 (1966).
[3]J. F. Holzrichter and J. L. Emmett, Appl. Opt. **8**, 1459 (1969).
[4]J. B. Trenholme and J. L. Emmett, "Xenon Flashlamp Model for Performance Prediction," in *Proceedings of Ninth International Conference on High Speed Photography* (Society of Motion Picture and Television Engineers, New York, 1970), p. 299.
[5]P. J. Walsh, W. Lama, and T. J. Hammond, J. Appl. Phys. **52**, 5476 (1981).
[6]C. H. Church, R. G. Schlecht, I. Liberman, and B. W. Swanson AIAA J. **4**, 1979 (1966).
[7]C. H. Church, R. G. Schlect, and I. Liberman, J. Quantum. Spectrosc. Radiat. Trans. **8**, 403 (1968).
[8]G. J. Linford, R. A. Saroyan, J. B. Trenholme, and M. J. Weber, IEEE J.Quantum. Electron. QE-15, 510 (1979).
[9]J. H. Kelly, D. C. Brown, and K. Teegarden, Appl. Opt. **19**, 3817 (1980).
[10]W. Lama, T. J. Hammond and P. J. Walsh, Appl. Opt. **21**, 654 (1982).
[11]S. I. Andreev, Sov. Phys. Tech. Phys. **20**, 635 (1976).
[12]V. M. Brabov and A. A. Shcherbakov, High Temperature **18**, 958 (1980).
[13]W. Lama and T. Hammond, Appl. Opt. **20**, 765 (1981).
[14]I. S. Marshak, *Pulsed Light Sources* (NRL Translation 1210, 1970).
[15]Y. Vitel, M. Skowronek, K. Benisty, and M. M. Popovic, J. Phys. D. **12**, 1125 (1979).
[16]L. P. Bradley and H. T. Powell, "Characteristics of Large Bore Xenon Flashlamps," Paper KB-3, 36th Gaseous Electronics Conference, Albany, New York, 1983. [Bull. Am. Phys. Soc. II **29**, 143 (1984)].
[17]E. I. Asinoviskii, N. A. Kolzlov and V. V. Fomin, High Temperature **11**, 843 (1973).
[18]A. P. Benson and P. B. Newell, "Performance of Large Xenon Flashtubes for Nd:Glass Disc Lasers", EG&G Technical Report No. B-4436, June 1975.
[19]Yu. G. Basov, J. Appl. Spectrosc. **35**, 943 (1981).
[20]M. Mitchener and C. H. Kruger, *Partially Ionized Gases* (Wiley-Interscience, New York, 1973).
[21]M. A. Gusinow and R. A. Gerber, Phys. Rev. A **5**, 1802 (1972).
[22]I. Amdur and E. A. Mason, Phys. Fluids **1**, 370 (1958).
[23]A. C. Jenkins and G. A. Cook, "Gas Phase Properties," in *Argon, Helium and the Rare Gases*, edited by G. A. Cook (Interscience, New York, 1961).
[24]W. F. Hagen, "Evaluation of the Iodine Laser," Max Planck Institut Fur Quantenoptik Report No. MPQ 52, Sept. 1981.
[25]D. K. Priest, "Study of Arc Growth and Lifetime Characteristics of 27 mm Bore Flashlamps," ILC Technology Report No. R-ILC-74-5, 1974.

[26]A. E. Orel, "Wall Losses In Flashlamps," 1982 Laser Program Annual Report, Lawrence Livermore National Laboratory, UCRL-50021-82, Aug. 1982.

[27]A. A. Shcherbakov, J. Appl. Spectrosc. **15**, 1193 (1971).

[28]V. M. Gradov and A. A. Shcherbakov, Opt. Spectrosc. **47**, 352 (1979).

[29]M. A. Biondi, "Recombination," in *Laser Plasmas*, edited by G. Bekefi (Wiley-Interscience, New York, 1976), pp. 125–158.

[30]Similar conclusions concerning the role of molecular ion formation and recombination as being arc confining mechanisms were obtained in studies of xenon arcs in hollow cathodes, F. G. Baksht and A. B. Rybakov, Sov. Phys. Tech. Phys. **28**, 909 (1983).

[31]L. P. Bradley and H. T. Powell "Flashlamp Characterization," 1982 Laser Program Annual Report, Lawrence Livermore National Laboratory, UCRL-50021-82, Aug. 1982.

[32]The behavior plotted in Fig. 16 has been observed experimentally by measuring the efficiency of exciting Nd:glass with Xe flashlamps as a function of angle. Since the Nd:glass absorbs radiation in discrete wavelength bands, its rate of excitation as a function of angle of incidence of radiation from the flashlamp is a sensitive measure of the spectral content of the pump radiation. See Ref. 31.

[33]D. C. Lorents, D. J. Eckstrom and D. Huestis, "Excimer and Decay Processes in Rare Gases," Stanford Research Institute, Report No. N00014-72-C-0457, Sept. 1973.

[34]T. F. O'Malley, Phys. Rev. **185**, 101 (1969).

[35]P. T. Rumsby and J. W. M. Paul, Plas. Phys. **16**, 247 (1974).

[36]J. W. Keto, R. E. Gleason, and G. K. Walters, Phys. Rev. Lett. **33**, 1365 (1974).

[37]R. A. Hass, "Group VI Laser System Analysis," Laser Program Annual Report-1977, Vol. 2, Lawrence Livermore National Laboratory, UCRL-50021-77, July 1978.

[38]D. Rapp and P. Englander-Golden, J. Chem. Phys. **43**, 1464 (1965).

[39]Analogy with Cs $(6s \rightarrow 6p)$ I. P. Zapesochnyi, E. N. Postor, and I. S. Alkedsaklen, Sov. Phys. JETP **41**, 865 (1976).

[40]D. Torr-That and M. R. Flannery, Phys. Rev. A **15**, 517 (1977).

[41]M. R. A. Rudge, Rev. Mod. Phys. **40**, 564 (1968).

[42]L. S. Frost and A. V. Phelps, Phys. Rev. **136**, A1538 (1964).